

A pore network model of porous electrodes in electrochemical devices

Andrea Gayon Lombardo*, Benedict A. Simon, Oluwadamilola Taiwo, Stephen J. Neethling,
Nigel P. Brandon

Royal School of Mines, Department of Earth Science and Engineering, South Kensington Campus, Imperial College London, London SW7 2AZ, United Kingdom



ARTICLE INFO

Keywords:

Pore network model
Electrode microstructure
Pore-scale modelling
Electrochemical devices
X-ray computed tomography

ABSTRACT

A computationally efficient pore network model (PNM) has been developed to incorporate the transport and electrochemical phenomena occurring within porous electrodes. This PNM is validated on a synthetic cubic structure and subsequently run on a network obtained from X-ray computed tomography (X-CT) images of a sample of commercial porous carbon paper commonly used in electrochemical devices. The carbon paper's physical characteristics (pore-size distribution, permeability, porosity and electroactive surface area) are discussed. The concentration distribution of active species is examined considering solely the transient convective and diffusive transport processes initially, and subsequently is compared to the concentration of active species when migration and reactive transport factors are included.

The results show non-uniformity in the concentration and pressure distributions in the electrode when considering the pure convective/diffusive transport processes. The migration and reactive processes are subsequently considered and are shown to be influenced by the rate in which the convective/diffusive flow permeates the electrode. A uniform steady decline in volume-averaged state of charge is shown, followed by a pore-scale non-uniform current density and state of charge distribution upon discharge. These results were obtained on a standard single core workstation highlighting the benefits of using a computationally inexpensive model.

1. Introduction

Electrodes constitute one of the main components in electrochemical energy storage and energy conversion technologies as they represent the sites where the major transport and reactive mechanisms occur [1]. Due to their importance in energy storage systems, understanding the multi-transport processes that occur within electrodes is crucial in order to improve their durability, increase the active surface area and aid in the design of more optimum systems [2–4].

It has been shown experimentally that further improvements in the electrode structure at a pore-scale level will lead to an improved power density [5–8]. However, experimental trial and error is expensive, time consuming and physically laborious. Therefore, it has become of high interest to employ mathematical modelling and simulation techniques to optimise and investigate electrode microstructure.

Electrochemical impedance spectroscopy (EIS) and transition line modelling (TLM) are important tools commonly implemented to investigate characteristics of porous electrodes. EIS is widely used [9,10], and is experimentally performed by measuring the response of an electrochemical system upon application of small oscillating currents or

potentials with varying frequency. The response is an impedance, Z , which can be plotted in several ways (Nyquist, Bode, Lissajous). Impedance of porous electrodes has been studied by many researchers including Huang and Sipioni [9,11]. In both of these papers, an equivalent circuit model (ECM) is used to describe the theoretical impedance response of each component. De Levie pioneered TLM, a subset of ECMs – which focuses specifically on the impedance associated within a porous electrode infiltrated by liquid electrolyte [12]. The main utility of this type of modelling is in predicting the availability of the electrochemically accessible surface area (which is not necessarily the same as the physical surface area) – the configuration of the porous electrode (e.g. pore-to-pore connectivity) is therefore taken into account. These methods have been used as the foundation to explain the movement of ions through electrolyte within porous electrodes [13]. Meyers et al. presented another important extension of this application by using these principles to describe the impedance associated with spherical intercalation particle movement through porous electrode materials [14]. While impedance studies are vital to understanding the resistances within an electrode, these resistances can also be analysed by implementing the governing transport phenomena equations over the cell domain.

* Corresponding author.

E-mail addresses: a.gayon-lombardo17@imperial.ac.uk (A. Gayon Lombardo), b.simon17@imperial.ac.uk (B.A. Simon), o.taiwo@imperial.ac.uk (O. Taiwo), s.neethling@imperial.ac.uk (S.J. Neethling), n.brandon@imperial.ac.uk (N.P. Brandon).

To date, most research has focused on modelling electrochemical energy storage and energy conversion technologies at a macroscopic level [15–24]. However, in these macroscopic models, complex electrode microstructure is usually overlooked and treated as a continuum where properties such as electrochemically active surface area, permeability and diffusivity are not based on real electrode geometry [25]. The reason for “over-simplifying” the microstructure is because electrodes are porous materials and, modelling flow and transport processes within these systems is mathematically complex and computationally expensive.

Models which directly use images of porous electrodes as their computational domains have been developed [25,26]. These pore-scale models offer the ability to distinguish between the solid electrode and the porous phase through which the electrolyte moves. This gives the advantage of capturing the effects of the electrode geometry on the battery performance [25,26]. Nevertheless, these models are computationally expensive and therefore often restricted to a small sub-volume of the entire electrode. It is therefore important to present a model with the ability to bridge the gap between a continuum scale description of electrodes and the detailed, but computationally restricted view offered by most pore-scale models. The pore network model offers a potential solution.

1.1. Transport modelling through porous media

Several mathematical techniques have been proposed to simulate the flow and transport phenomena through porous media. The three main approaches are: continuum models, direct numerical simulations (DNSs), and pore network models (PNMs) [27].

Continuum models are formulated based on the assumption of a representative elementary volume (REV) over which physical micro-properties, such as porosity and tortuosity, are volume-averaged. From this assumption, velocity and pressure profiles are then defined by phenomenological relationships (*i.e.* Darcy's law, Brinkmann or modified Navier-Stokes equations), and finally transport equations are solved with numerical discretisation methods (finite volume method (FVM), finite difference method, etc.) [27,28].

DNS approaches perform simulations over the complex pore geometry obtained directly from X-ray computed tomography (X-CT) images. The porous microstructure is represented as a structured or unstructured numerical mesh, or simply as a Cartesian grid, depending on the type of DNS applied. DNSs can be classified as (1) grid-based simulations that employ the finite volume method (FVM) to solve the governing partial differential equations [15,29], or; (2) particle-based methods such as the Lattice-Boltzmann method (LBM) [30] and smoothed particle hydrodynamics [31].

PNMs represent a major pore-scale modelling approach, where the porous medium is represented as a simplified network of interconnected pores and throats [32,33]. In these models, the details of individual pores are ignored, but the complete topology of the pore space is represented [28].

1.1.1. Examples of transport modelling through porous media

In comparing a continuum model using the FVM in conjunction with a PNM, Rebai and Prat outlined the shortcomings associated with continuum models typically used to describe two-phase flow in gas-diffusion layers leading to a poor approximation of water distribution [27]. These problems are due to the lack of length scale separation and are rooted in the assumption of the existence of a (REV) much smaller than the porous domain. In this context, García-Salaberri et al. used the LBM to compute the effective mass transport properties (*i.e.* permeability, diffusivity, electrical and thermal conductivity) in different carbon fibre papers (CFPs) and concluded that the macro-homogeneous models of CFPs can lead to non-negligible errors in their predictions [34]. One major conclusion of this work is that a CFP medium is too highly heterogeneous to be treated as a continuum, since its

microscopic properties greatly diverge depending on the plane through which they are analysed. Furthermore, the authors state that a REV, normally used as a basis in macro-homogeneous continuous models, cannot be defined in CFPs due to the lack of a well-defined separation between pore and volume-averaged scales (only one order of magnitude different) – this is attributed to the CFP's very small thickness and is in agreement with the findings of Rebai and Prat [27].

In terms of pore-scale models, Yang et al. used a ‘benchmark’ 3D complex porous medium problem to perform comparative flow and solute transport simulations of four different modelling approaches: FVM (grid-based), LBM (particle-based), smoothed particle hydrodynamics and PNM [28]. Quantitative comparisons between the models yielded largely similar microscopic (pore scale velocities) and macroscopic (permeability, breakthrough curves, effective dispersity) measures. Discrepancies are thought to lie in the difference in meshing and grid resolution.

Among the conclusions reached in all the studies mentioned here, is that PNM demonstrate a far superior computational efficiency relative to DNSs due to their ability to simplify microstructure and electrode topography (in the comparison made by Yang et al. the benchmark problem was solved in 61.07 h using an LBM approach on two TESLA K40c GPGPU supercomputers while solving a PNM on a standard Intel Core i7-4790 CPU only took 45 s) [28,32].

The methodologies mentioned so far are widely used to solve the flow and transport processes through porous media. However, their application can be extended to analysing porous components of electrochemical systems such as electrodes or gas diffusion layers (GDLs). The following section aims to demonstrate these methodologies in an electrochemical context.

1.1.2. Examples of application of transport modelling to electrochemical systems

A first approach for analysing multiphase flow in electrochemical systems at a pore-scale was presented by Park et al., who proposed a microscopic model based on the LBM to analyse the two-phase flow distribution in the GDL of a PEM fuel cell [35]. This work implemented the LBM to investigate the effect of the tow orientation and effective permeability of carbon fibres in a GDL.

As an attempt to introduce a less computationally expensive model, Gostick et al. presented a PNM for analysing water formation in the GDL of a PEM fuel cell [36]. The authors outline a methodology for representing the microstructural properties of SGL 10BA and Toray 090 through a hypothetical cubic framework. Although this approach represents the experimental data of permeability and diffusivity with accuracy, it does not represent the actual geometry and topology of the porous materials. The advantage of this method lies in the ease with which it can be combined with a macroscopic model of a complete fuel cell. As an extension of this work, Aghighi et al. implemented a microscopic model coupled with a macroscopic one to model a complete PEM fuel cell [37]. In their work, the multiphase transport of species in the GDL is modelled as a PNM and a continuous model is applied for representing the membrane and electrode catalyst layer. The aforementioned approaches have been implemented to analyse PEM fuel cells porous components such as GDL and catalyst layer. Recently Banerjee et al. implemented a PNM to model the multiphase flow of electrolyte in carbon fibre electrodes for a vanadium redox flow battery (VRFB). This work analyses the transient permeation of electrolyte in different types of commercially available CFPs [38].

Previous approaches have been implemented for analysing a single or multi-phase non-reactive flow, through porous media. However, only Qiu et al. have extended the applicability of microscale models to analyse the effect of real microstructure in the mass and reactive transport processes within porous electrodes [25,26]. In their work, the LBM is used to solve the flow equations and with the resulting flow, alongside the FVM, the mass transport processes are simulated over a real X-CT image.

1.2. Outline of the present work

The present work outlines a novel methodology for implementing a PNM approach to study the multiphysics involved in porous electrodes. In addition to accounting for flow characteristics and reactive transport processes, this model examines pore current and electrolyte concentration at different overpotentials.

This work is structured as follows: In Section 2 the transport equations implemented in this work are introduced, furthermore the possible boundary conditions are explained, and finally an iterative algorithm for solving the equations is described (with supplement in Appendix 1). Section 3 validates the methodology by implementing the model over a hypothetical PNM, built with the open-source software Open PNM [39], to represent a Toray 900 carbon paper (previously validated by Gostick et al. [36]). As a case study, an X-CT image from a Toray 900 carbon paper sample, commonly used as an electrode material for various electrochemical technologies, is analysed. The pore-network was extracted from the segmented image using the Amira-Avizo 9.2.0 software (Avizo) and the numerical model was implemented over the constructed PNM.

2. Methodology

The PNM approach presented in this work comprised three main steps which will be detailed below. First, the pore network structure was generated from two sources, namely open source data provided by OpenPNM [39], and reconstructed 3D geometry obtained from X-CT images. Having obtained the pore-scale topology of the network, the pressure and velocity profiles were calculated by solving the Stokes flow equation in each pore. Subsequently, the computed velocity field was integrated with the mass and charge transport equations to obtain the concentration and potential field across the network. In order to simultaneously solve the coupled potential and species concentration at each pore, an iterative method was employed, with the concentration and potential being simultaneously updated until a convergence limit was achieved. As these are dynamic simulations, this procedure was repeated at each time-step.

In the following sections, and indeed throughout the rest of the paper, terms contained within Fig. 1 will be referred to in the derivations and discussions.

2.1. Fluid transport equations for PNMs

In this work, a PNM approach was implemented for simulating the flow through the connecting throats in the network. As established by other authors [40,41], in a PNM, the flow through each throat connecting two pores is analogous to the analytical solution of the steady-state Navier–Stokes equation for the flow through a pipe given that the flow is considered to be at low Reynolds number (*i.e.* $Re \ll 1$). The

pressure and velocity fields are obtained by assuming a single pressure value per node, and enforcing a volume balance over each pore as given by Eq. (1):

$$\sum_{j=1}^{N_{th}} q_{i,j} = \sum_{j=1}^{N_{th}} q_{ij}(P_i - P_j) = 0 \quad (1)$$

where P_i is the pressure at pore i , q_{ij} is the flow between pores i and j , g_{ij} represents the hydraulic conductivity of the throat connecting pores i and j , and N_{th} is the number of throats connected to pore i .

The hydraulic conductivity (g_{ij}) is a factor that represents the resistance to the electrolyte flow from one pore to its neighbouring pores imposed by the connecting throat. It is dependent on the size and length of the throat and will vary depending on the shape of the throat's cross-sectional area. In this work, the throat geometry is assumed to be cylindrical, and thus the hydraulic conductivity is defined as:

$$g_{ij} = \frac{\pi r_t^4}{8\mu L} \quad (2)$$

where r_t refers to the throat equivalent radius, and μ is the electrolyte viscosity.

The macroscopic flow rate (*i.e.* Q_T , below) can be obtained by adding the flux over the boundary pores of the network along the main flow direction, given by Eq. (1). From Darcy's law, the bulk permeability can be computed through back-calculation with Eq. (3):

$$Q_T = \frac{KA(P_{in} - P_{out})}{\mu L} \quad (3)$$

where K is the bulk permeability, A is the cross-sectional area of the electrode in the main direction of flow, L is the total length of the network, P_{in} and P_{out} refer to the inlet and outlet pressures at the boundaries respectively [36,40–44].

The formulation of the flow equation is built upon the following assumptions:

- The electrolyte consists of a single-phase, Newtonian, incompressible fluid;
- The fluid in the bulk is under creeping flow conditions ($Re \ll 1$);
- The viscosity of the electrolyte is uniform throughout the electrode; and,
- In this work, the pores are considered to be spheres and the throats are cylindrical. This assumption can be relaxed as it is not a necessary condition of the model. The geometric parameters from Eq. (2) can be manipulated to model pores and throats with different shapes.

2.2. Species (mass) transport equations for PNMs

A methodology for solving the convective-diffusive-reactive transport of species in a pore network model has been previously introduced

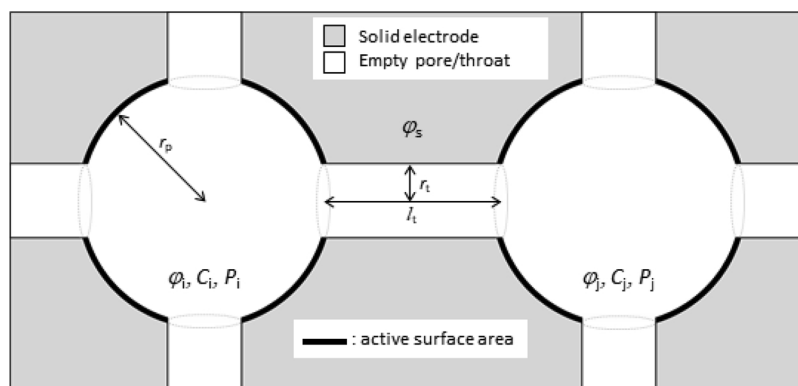


Fig. 1. Electrochemical and geometric properties of the pore network model.

for various applications (*i.e.* adsorption, carbon capture and storage, biomass growth) as the mixed-cell-method (MCM) [40–43,45,46]. This method is based on the assumption that the concentration of species at the bulk of the pore is the same throughout the extent of the pore, thus the concentration at the inlet of each throat attached to a certain pore is the same.

From the same principle that derived the MCM for reactive transport, this work presents a methodology for obtaining the transient distribution of species within the electrode. In this case, the flux density of species is determined by diffusion and convection, and an additional term due to electrophoretic transport, defined as migration, is introduced. This model is based on the following assumptions:

- The dilute solution approximation is considered in the transport of species through the porous phase. This assumption implies that the concentrations of species are low enough that their fluxes do not have an impact on the flow of the solvent; and,
- Since this is a pore-scale model, the concentration of species at the bulk of each pore (C_b^l) is taken to be the same as the concentration at the boundary of the active surface area (C_s^l). It must be emphasised that this condition can be relaxed through the implementation of a mass transport resistance in the equations corresponding to the chemical reaction (Eq. (5)) to relate C_b^l with C_s^l .

The transport of species due to convection, diffusion, migration and electrochemical reaction at each pore ' i ' is defined as:

$$V_i \frac{dC_i^l}{dt} = \sum_{j=1}^{N_{th}q < 0} C_i^l q_{ij} + \sum_{j=1}^{N_{th}q < 0} C_i^l q_{ji} + \sum_{j=1}^{N_{th}} D_L A_{ij} \frac{(C_j^l + C_i^l)}{l_{ij}} + \sum_{j=1}^{N_{th}} z_l D_L C_i^l \frac{F(\varphi_j - \varphi_i)}{RT A_{ij}} + S(C_i^l) \quad (4)$$

where V_i is the volume of pore i ; C_i^l the concentration of species l in pore i ; q_{ij} , l_{ij} and A_{ij} the flow rate, length and cross-sectional area of the throats connecting pores i and j , respectively. D_L represents the longitudinal dispersion coefficient, given by the equation $D_L = D_e + \alpha v^b$, where D_e represents the effective diffusion coefficient of the medium, α is the dispersivity, b a constant and v the velocity of the fluid. For porous media, D_e is given as a function of the tortuosity factor and the porosity, most commonly defined by the Bruggeman relation. The ratio of convection to diffusion is given by the Peclet number, $Pe = vd_p/D_e$ where d_p is a characteristic length of the porous media (in this work d_p is the pore diameter). When the Pe is of the order of 1, the dispersion coefficient reduces to D_e . At very high flow rates however, $Pe \gg 1$, the dispersion coefficient becomes a function of the fluid velocity [47]. In this work the Pe was calculated in all cases and was of the order of 1 in most pores. Based on this and for simplicity D_L reduces to D_e . Since the present model is a pore-scale model, the effective diffusivity D_e reduces to a diffusion coefficient D for each component in the electrolyte, since the tortuosity and porosity are accounted for directly in the network topology.

The first two terms on the RHS of Eq. (4), represent the convective transport into and out of each pore; the third term on the RHS shows the transport due to diffusion, the fourth term represents the migration due to electrophoretic transport of species; and S represents the source/sink term in concentration due to the electrochemical reaction. For the reduced active species, the source term is defined as i_{BV}/F and for the oxidised active species the source term is defined as $-i_{BV}/F$. In both cases i_{BV} is the transfer current obtained from the Butler–Volmer equation, as explained in the following subsection.

2.2.1. Electrochemistry

From the mass transport Eq. (4) solved at each pore, the source/sink term S represents the flux of species l averaged over the active surface

area. The flux obtained due to the formation/consumption of species at the pore wall is determined by the current (i_{BV}) transferred at each pore, given by the Butler–Volmer Eq. (5):

$$i_{BV} = i_0 \left[\exp\left(\frac{\alpha_z F \eta_a}{RT}\right) - \exp\left(-\frac{\alpha_z F \eta_a}{RT}\right) \right] \quad (5)$$

where i_{BV} is the current transferred at each pore in the anode, z is the number of electrons involved in the electrochemical reaction, α_z is the anodic charge transfer coefficient for the electrochemical reaction, i_0 is the exchange current at each pore in the anode, defined as:

$$i_0 = S_A F k_a (C_R)^{\alpha_z} - (C_{Ox})^{\alpha_z} \quad (6)$$

where k_a is the reaction constant for the heterogeneous reaction, C_R and C_{Ox} are the concentration of species involved as a redox couple in their reduced and oxidised form respectively, and S_A is the active surface area of each pore. The activation overpotential η_a due to the electrochemical reaction at the anode is defined as:

$$\eta_a = \varphi_s - \varphi_e - E_a \quad (7)$$

where $\varphi_s - \varphi_e$ represents the potential difference between the solid phase (*i.e.* carbon fibres) and the electrolyte; E_a represents the equilibrium potentials calculated with the Nernst Eq. (8):

$$E_a = E_a^0 + \frac{RT}{F} \ln\left(\frac{C_{Ox}}{C_R}\right) \quad (8)$$

where $E_{0,a}$ denotes the standard equilibrium potential of the redox couple involved in the reaction.

2.3. Charge transport equations for PNMs

In the porous electrode, the current is produced within the two phases, namely the electrolyte (ionic current) occupying the porous phase and the carbon fibres (electronic current). The methodology presented in this work for obtaining the transport of charge across the network is based on the following assumptions:

- The solution is electrically neutral; and,
- The electrode, comprising of carbon fibres is highly conductive, compared to the electrolyte flowing through the porous phase. The potential difference across the solid matrix is therefore negligible ($\nabla \varphi_s = 0$).

In the case of the electrolyte, the ionic current transferred between pores can be obtained by imposing a charge balance at each pore, based on the assumption of a diluted solution:

$$\frac{\partial}{\partial t} F \sum_l^{nc} z_l C_l = -\nabla \cdot R \sum_l^{nc} z_l \mathbf{N}_l + F \sum_l^{nc} z_l S_l \quad (9)$$

where \mathbf{N}_l is the molar flux of ionic species defined by the Nernst–Plank equation, $z_l F$ is the charge per mole of species l , and nc is the total number of species in solution. Following the condition of electro-neutrality for the electrolytic solution (*i.e.* $\sum_l^{nc} z_l N_l = 0$), the LHS of Eq. (9), corresponding to the accumulation of charge, is zero. Therefore, the sum of charge transported by migration due to a potential difference into/out of one pore (corresponding to the first term on the RHS of Eq. (9)) must be equal to the charge transferred outside the pore into the solid matrix due to the electrochemical reaction (corresponding to the second term on the RHS of Eq. (9)).

The current transferred at the interface of the active surface area (i_{BV}) is computed with the Butler–Volmer equation. The total current transferred at each pore produced by the migration of species from one pore to the other (i_t) is defined as:

$$i_t = -\nabla \cdot \left[F^2 \nabla \varphi \sum_l^{nc} z_l^2 \frac{D_L C_l}{RT} + F \sum_l^{nc} z_l D_L \nabla C_l \right] \quad (10)$$

To obtain an expression analogous to the MCM for the charge transport at each pore, a volumetric integral of Eq. (9) is performed. The resulting expression represents the charge transfer into/out of each pore due to a potential difference between pores:

$$i_t = -F \sum_l^{nc} z_l \left[z_l D_L C_i^l \frac{F}{RT} \left[\sum_j^{N_{th}} A_{ij} \frac{(\varphi_j - \varphi_i)}{l_{ij}} \right] + D_L \left[\sum_j^{N_{th}} A_{ij} \frac{(C_j^l - C_i^l)}{l_{ij}} \right] \right] \quad (11)$$

where C_i^l is the concentration of species l in pore i ; φ_i is the potential of the electrolyte in pore i ; l_{ij} and A_{ij} are the length and cross-sectional area of the throats connecting pores i and j respectively.

2.4. Boundary conditions

This section presents the available boundary conditions that can be implemented in the present model to solve the equations of flow, mass and current transport defined in the previous section. The implementation of each boundary condition is determined by the specifications of the system studied.

2.4.1. Boundary conditions for flow transport

To determine the electrolyte flow profiles across the network, two possible boundary conditions can be established. The first case defines the flow of electrolyte as driven by a pressure gradient between the inlet and outlet pressures. Therefore, constant pressures are specified at the inlet (P_{in}) and outlet (P_{out}) pores as Dirichlet boundary conditions. The second case establishes a flux at the inlet or outlet, and a Dirichlet boundary of pressure on the opposite side. The first case is more realistic since the inlet and outlet pressures are usually known variables.

2.4.2. Boundary conditions for species transport

In all cases, an assumption of constant concentration at the inlet pores is established. For the outlet pores, the following conditions can be implemented to obtain the concentration profiles across the network:

Case I: Dirichlet boundaries are considered at the inlet and outlet pores, thus the concentrations at the inlet and outlet boundaries are fixed and unchanged throughout the simulation. This assumption is valid for the cases in which the conversion of species is known and therefore the concentration of species at the inlet and outlet pores are set constant. Case II: A Dirichlet boundary is established at the inlet pores and a Newman boundary condition of zero diffusive flux out of the system is established at the outlet throats. This condition must be implemented for the cases in which there is no information available regarding the conversion of species.

2.4.3. Boundary conditions for charge transport

The cell can be considered to be operated at either potentiostatic or galvanostatic conditions. For the case of a potentiostatic operation, electrolyte potentials are fixed at the inlet and outlet pores as Dirichlet boundaries, and the electrolyte potential in each pore across the network is recalculated at every time-step in the transient concentration. For the case in which the cell is assumed to be operating under galvanostatic conditions, the potentials at one of the walls are fixed as a Dirichlet boundary and the potentials at the other wall are recalculated iteratively to fit the external current density applied to the electrode (*i.e.* $\varphi_s = 0$). A constant distribution of potential along the solid matrix is considered, since the fibre is assumed to be significantly more conductive than the electrolyte. This assumption is based on the experimental data presented by Gandomi et al. [20].

2.5. Iterative algorithm

The core part of this work is the implementation of a framework based on a PNM approach to solve the coupled mass and charge

transport equations that occur at the pore phase within the electrode. Each of the main steps involved in the algorithm for solving the flow, concentration and current profiles are defined in detail in this section.

As a first step, the steady-state Stokes flow equation was applied to obtain the pressure and flow field across the network. For this, the system of linear equations, given by expression [1], was solved with the implementation of an iterative successive over-relaxation (SOR) method. Since the velocity field only depends on the geometrical topology of the microstructure, a steady-state pressure drop was assumed throughout the transient concentration simulation. The pressure difference between the inlet and outlet was specified such that the $Re \ll 1$ and the average velocity was comparable to the values used in continuum models.

Once the flows across each throat were known, an iterative algorithm was implemented to compute the transient distribution of concentrations throughout the network. This algorithm is iterative for calculating the potentials at each pore and explicit for calculating the concentration at each time-step. For this, an explicit Euler scheme was implemented for discretising Eq. (4) as follows:

$$\begin{aligned} C_{i,l}^{n+1} = C_{i,l}^n &+ \frac{\Delta t}{V} \left[\sum_{j=1}^{N_{th},q<0} C_{i,l}^n q_{ij} + \sum_{j=1}^{N_{th},q>0} C_{j,l}^n q_{ij} \right] \\ &+ \frac{\Delta t}{V} \left[\sum_{j=1}^{N_{th}} D_L A_{ij} \frac{(C_{j,l}^n - C_{i,l}^n)}{l_{ij}} \right] \\ &+ \frac{\Delta t}{V} \left[\sum_{j=1}^{N_{th}} z_l D_L C_i^l \frac{F}{RT} A_{ij} \frac{(\varphi_j^n - \varphi_i^n)}{l_{ij}} \right] + \frac{\Delta t}{V} \left[\frac{i_{BV}^n}{F} \right] \end{aligned} \quad (12)$$

From Eq. (12) it is seen that the transport of species from pore to pore is influenced by the migration and source terms, corresponding to the last two terms on the RHS of the equation respectively. This implies that the movement of active species is affected by the electrolyte potential at each pore (*i.e.* in the source term), as well as the electrolyte potential of the neighbouring pores (*i.e.* in the migration term). For this reason, in order to obtain the distribution of potentials and concentrations across the network, the species and charge transport equations (*i.e.* Eqs. (11) and (12) respectively) were solved simultaneously for every pore at each time-step. Thus, each time-step will correspond to a specific concentration and potential distribution. At every time-step, the potential distribution was obtained iteratively with a SOR method, where the error function was defined as the absolute average deviation (AAD) between i_t and i_{BV} at each pore:

$$ADD = \frac{1}{np} \sum_i^{np} ||i_{t,i}^n - i_{BV,i}^n|| \quad (13)$$

Once the electrolyte potential distribution was obtained, the migration and source terms of Eq. (12) (*i.e.* the last two terms) were calculated at each pore. Finally, the concentrations at each pore were calculated explicitly with Eq. (12), providing the new concentrations (*i.e.* C_i^{n+1}) for the following time-step. Based on the new concentration profile, the potentials for the following time-step were recalculated using the same process and convergence condition as defined before. This process of solving the potentials iteratively and updating the concentrations was performed for every time-step until a maximum time limit was achieved. A schematic of the solution algorithm introduced in this work is shown in Appendix 1.

The convergence criteria for calculating the pressure field was defined as the average residual of the sum of all flows (obtained from Eq. (1)), non-dimensionalised against the total sum of the absolute flows in all throats. The simulation converged when the average residual was less than or equal to 1×10^{-12} . The convergence criteria for the potential fields was obtained with Eq. (13), where the simulation converged when the AAD from Eq. (13) was less than or equal to 1×10^{-8} A. The implementation of the numerical algorithm requires the

following inputs: physical parameters of the electrolyte (e.g. diffusivity, **Table 1**), initial SOC, inlet velocity, outlet pressure, external current density or boundary potentials, input file of the reconstructed pore network with data including pore volume/position and throats radius/length and connecting pores indexes/identities.

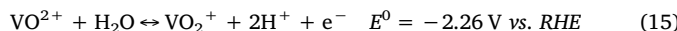
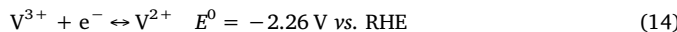
The implementation of a fully explicit Euler scheme for the volume-integrated transport equation for convective, diffusive, reactive and migration transport had to be verified with its corresponding analytical solution. Results are shown in Appendix 2. The program developed in this work is written in C++ and implemented on an HP workstation with the following specifications: Intel® Xeon® CPU E5-166-v3.

3. Results and discussion

3.1. Implementation of methodology in a vanadium redox flow battery

For the purpose of proving the methodology developed in this work, the anode couple (Eq. (14)) based on a VRFB was used. Vanadium chemistries are the most intensely studied electrochemical systems in RFB development and most commercially mature [48,49]. Thus, significant progress in VRFBs cell power density has been made over the last 30 years [50–52].

VRFB electrolyte chemistries utilise all four stable oxidation states available to vanadium. They are V²⁺/V³⁺ at the negative electrode (anode) and VO²⁺/VO₂⁺ (V⁴⁺/V⁵⁺) at the positive electrode (cathode). Complicated kinetic and mechanistic equations are omitted in the following simplified electrochemical couples [20].



To achieve target costs for commercialisation [53,54], two main challenges need to be addressed: (1) lowering the cost of electrolytes, and; (2) developing high-powered RFB systems. One of the main barriers in tackling the later challenge lies in electrode performance, and therefore this work focuses here.

Table 1 presents the physical parameters corresponding to the electrochemical reaction undertaken by the redox couple V²⁺/V³⁺ at the anode. These parameters were implemented in the species transport equations defined previously.

Table 1
Physical parameters for the mass transport Eq. (5) from literature [25,55–57].

Parameter	Symbol	Value	Units
Anodic transfer coefficient	α_-	0.5	—
Cathodic transfer coefficient	α_+	0.5	—
Standard reaction rate constant: anode	k_a	1.7×10^{-7}	m s^{-1}
Equilibrium potential: anode	$E_{0,a}$	-0.255	V
Temperature	T	298	K
Diffusivity of V(II)	$D_{(\text{VII})}$	2.4×10^{-10}	$\text{m}^2 \text{s}^{-1}$
Diffusivity of V(III)	$D_{(\text{VIII})}$	2.4×10^{-10}	$\text{m}^2 \text{s}^{-1}$

3.2. Model verification

To verify the implementation of a PNM approach to represent a carbon paper electrode, a critical parameter to understand is the effect of the active surface area on the electrode potential. For this, a hypothetical network was built using the open-source software OpenPNM, specifically the Toray090 module, to represent a carbon paper electrode [39]. The module for building a Toray090 architecture from OpenPNM was previously verify in terms of permeability and diffusivity elsewhere [36], and therefore was used as basis for this work. The iterative algorithm presented in this work was applied over the hypothetical network to simulate the negative half-cell of a VRFB. The results of this simulation were compared to the results of the 2D half-cell continuum

model of the anodic half-cell of a VRFB presented by You et al. [55]. The hypothetical network was built as a cubic structure, consisting of 2336 pores and 4048 throats, with an architecture specially designed to preserve the geometric parameters and specific surface area used by You et al. [39,55]. These parameters are reported in **Table 2**.

Table 2
Parameters defining pore network model.

Description	Symbol	Value	Units
Specific surface area	A_e	16,200	m^{-1}
Half-cell width	L	0.003	m
Flow velocity	u_{av}	0.00219	m s^{-1}
Average pore size	—	3.90×10^{-15}	m^3
Number of pores	N_p	2336	—
Number of throats	N_t	4048	—
Total vanadium concentration	C_{tot}^0	1500	$\text{m}^3 \text{s}^{-1}$
External current density	$-J_{ext}$	-400	A m^{-2}
Equilibrium potential	E^0	-0.255	V

The methodology presented in this section for validating the model is analogous to the simplified structure presented by Qiu et al. [25]. This approach is based on the charge conservation between the applied current density and balance of current within the pore phase represented by the pore network. The following assumptions were made for validating this methodology:

- The solid fibres are considered significantly more conductive than the electrolyte, therefore the potentials in the solid matrix are considered constant throughout the electrode (i.e. $\varphi_s = 0$);
- The VRFB is operated under steady-state conditions at every state-of-charge (SOC) considered;
- The effect of side reactions are negligible;
- Only the half reaction of the negative electrode (anode, denoted ‘a’ in following equations) is considered; and,
- From the solution of the flow profiles, the average velocities are obtained and the Pe calculated. In all cases, the Pe was of the order of 1, therefore, the D_L from the mass transport equation is reduced to the diffusion coefficient of the vanadium species (i.e. $D_{V(II)}$, $D_{V(III)}$).

3.2.1. Boundary conditions for flow transport

Dirichlet boundary conditions of pressure were implemented at the inlet and outlet pores to obtain an average velocity of 0.00219 m s^{-1} , equivalent to experimental data and the continuum model presented by You et al. [55].

3.2.2. Boundary conditions for species transport

The concentration of species within each pore was determined by the solution SOC within the electrode, defined as:

$$\text{SOC} = \frac{C_{II}}{C^0} \quad (16)$$

where C_{II} corresponds to the concentration of V(II), and C^0 is the total concentration of vanadium species (i.e. V(II) and V(III)) in solution. Since the system is considered to be operating under steady-state at each SOC analysed, Dirichlet boundary conditions of concentration were implemented at the inlet and outlet pores.

3.2.3. Boundary conditions for current transport

Based on the assumption of a perfect mix at each pore, the potentials in the electrolyte (φ_e) represent the potential at the solid–liquid interface, thus a distribution of potentials across the network must exist at each SOC. In order to implement a simulation under galvanostatic conditions to compare against the data gathered by You et al. [55], the potential at one boundary of the PNM was set constant, while the potential at the other boundary was calculated iteratively until the

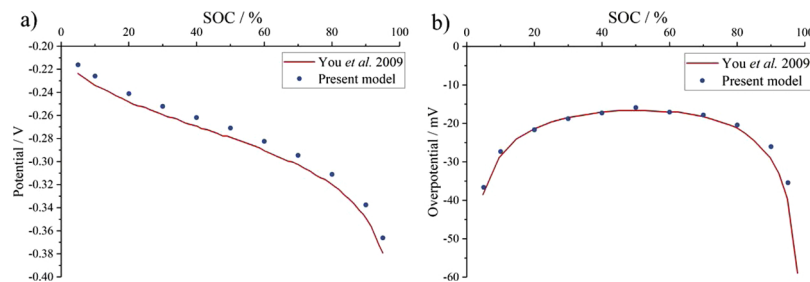


Fig. 2. Plots showing graphical validation of cell discharge at 400 A m^{-2} compared with literature results [55].

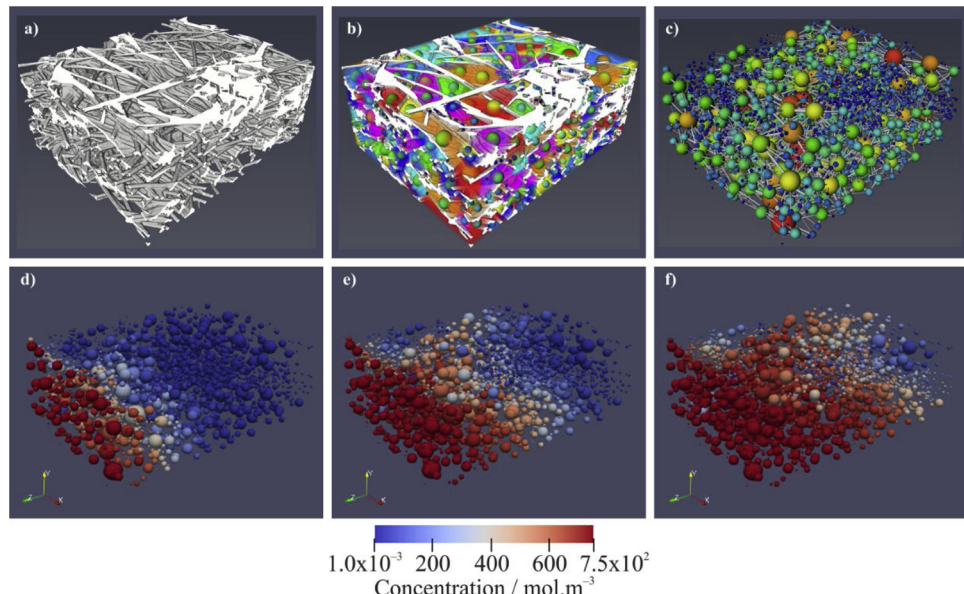


Fig. 3. Overview of pore network extraction and operation: (a) X-CT segmented image, (b) pore fractions with inserted pore network, (c) standalone pore network, (d–f) 3D example of simulation.

calculated external current density ($J_{ext,calc}$) matched the desired external current density (J_{ext}). The calculated external current density is derived from the charge conservation in the network as follows:

$$J_{ext,calc} = \frac{\sum_{i=1}^{Np} i_{BV,i}}{\sum_{i=1}^{Np} S_{A,i}} \cdot A_e L \quad (17)$$

where $S_{A,i}$ is the surface area of pore i , $i_{BV,i}$ is the current at pore i , A_e is the specific surface area of the PNM and L is the electrode thickness or half-cell width for this case. As stated in the iterative algorithm, the current at each pore obtained by the Butler–Volmer Eq. (5) must be equal to the current obtained due to transport of charged species (Eq. (11)); thus, the calculation of the external current density represents a secondary iteration that encompasses the primary iterative algorithm.

3.2.4. Results and comparison

The steady-state solution of the pressure and flow fields converged in 4 s, and the coupled charge and species transport distributions converged after 14 min for each time-step in the simulation, using a single core of a HP workstation: Intel® Xeon® CPU E5-166-v3.

The potential difference between the solid phase and the electrolyte (i.e. $\varphi_s - \varphi_e$) represents the potential drop across the electrode active surface. These values are obtained as outputs from the numerical algorithm and averaged for all pores to obtain the electrode potential averaged throughout the volume of the electrode. The overpotential at each pore is calculated with Eq. (7) based on the output data of the potentials and concentration distributions and the equilibrium potentials calculated with Eq. (8).

Fig. 2(a) shows the simulated electrode potentials for the negative half-cell of a VRFB as a function of the SOC for an applied current density of 400 A m^{-2} . **Fig. 2(b)** presents the averaged overpotentials obtained from the PNM simulation for the negative electrode at galvanostatic charge at 400 A m^{-2} . The results are compared with the 2D model presented by You et al. [55] which was previously validated with experimental data with a 1% error making it reliable for validation purposes. Compared to those results, the present PNM model returns an absolute average error of 3.02% for the half-cell potentials and of 4.06% for the overpotentials.

3.3. Case study: Toray 090 from X-CT image

As a case study for the implementation of the numerical methodology presented in this work, the simulation was tested over a pore network extracted from a segmented X-CT image of Toray 090 carbon paper sample. For this study, the carbon paper (typically used as electrode in VRFBs) was imaged using a laboratory X-ray computed tomography system (Nanotom 180 S, GE Phoenix, USA). The technique applied for segmentation and reconstruction of the image is explained elsewhere [58], but in short, a 3D median smoothing filter was applied to the reconstructed volume to reduce the image noise. Threshold-based image segmentation of the volume was then performed to isolate the carbon fibres from the pore/electrolyte phase (Fig. 3) [58]. Characterisation of the electrode in terms of physical size is shown in Table 3.

The pore network of a Toray 090 paper was extracted using Avizo software and is based on the “Maximal Ball” algorithm [32]. The pore

Table 3
Toray 090 sample electrode dimensions.

Electrode	x	y	z	Resolution
Toray (voxels)	678	330	840	0.65 μm per voxel
Toray (μm)	440.7	214.5	546.0	–

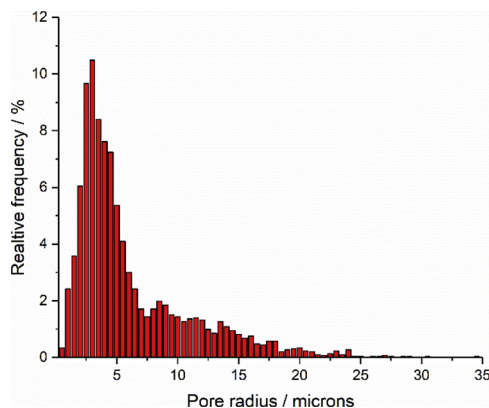


Fig. 4. Pore size distribution histogram representing the pore network extracted from an X-CT image of a Toray 090 sample.

network is comprised of 2928 pores and 8510 throats, with a pore size distribution shown in Fig. 4.

3.3.1. Permeability, porosity and active surface area calculations

The condition to initialise the iterative pressure solver at each pore was set to $P_i = 0$. The solution of the system of linear equations yielded by the application of Eq. (1) in each pore, provides the flow rate through each of the input and output throats. The sum of all the input flows gives the total flow rate through the network (Q_T). The permeability of the network is calculated using Eq. (3) in the largest and the smallest face. The area (A) normal to the flow direction and length (L) parallel to the flow direction were calculated from the X-CT images. From the solution of the flow profiles, the average velocities are obtained at each throat and the Pe calculated. The average Pe was 1.63, therefore, the D_L from the mass transport equation is reduced to the diffusion coefficient of the vanadium species (i.e. $D_{V(II)}$, $D_{V(III)}$); these values are reported in Table 1.

In all the simulations performed in this work, the smallest and the largest faces of the electrode were set as boundaries and the absolute permeabilities were calculated through both planes. The values of the calculated absolute permeabilities are reported in Table 4 with the two values of viscosity for the vanadium solution reported on the literature [25,55]. A comparison is shown between the permeabilities calculated

Table 4
Permeability data ($\times 10^{12} \text{ m}^2$) of a sample of Toray 090 calculated from pore network model using different viscosities [25,55], compared with literature [36].

Plane	Model	
	($\mu = 4.928 \times 10^{-3} \text{ Pa s}$) [55]	($\mu = 2.5 \times 10^{-3} \text{ Pa s}$) [25]
Smallest face	16.16	8.20
Largest face	11.44	5.80
Literature values based on Toray 090 [36]		
Experimental		Model
K _x	15	14
K _z	9.0	9.5

with the pore-network extracted from an X-CT scan of Toray 090 and the values reported by Gostick et al. [36], both experimental and modelled for a Toray 090 carbon paper. It is shown that the values reported in the literature are similar and within the same order of magnitude as the values calculated in this work. These results show that the electrode topology determined by the pore-network extracted with Avizo is representative of the Toray 090 paper micro-structure in terms of flow. The porosity, given by Avizo was 68.42% and the specific surface area was calculated as $41,062 \text{ m}^{-2}$.

3.3.2. Boundary conditions

As previously stated in Eq. (4), the transient distribution of species is determined by the interplay of four main factors: convection, diffusion, migration and electrochemical reaction. The contribution of each factor will be determined by thermodynamic and kinetic properties of the electrolyte, as well as by geometric parameters determined by the microstructure and topology of the electrode. To understand the effect of each contributing factor, they were analysed separately as follows: the effect of the electrolyte permeation due to convection and diffusion were analysed first as if the system was not electrochemically reactive. Following this, the additional transient distribution of species due to migration and electrochemical reaction were included.

3.3.2.1. Boundary pores definition. For determining the boundary pores (i.e. inlets and outlets) of the pore network obtained from the X-CT image, an algorithm was developed as follows: the maximum length of X-CT image in each dimension was calculated by measuring the largest perpendicular distance between the two furthest-most pores (in each dimension). Using this, a virtual film spanning each face of the image, with a thickness of 1% of the total thickness of the 3D image, was calculated. If any given pore volume overlapped with this virtual film, it was taken to be a boundary inlet or outlet pore.

3.3.2.2. Boundary conditions for flow transport. To obtain the flow distribution through the network, Dirichlet boundary conditions of pressure were set at the inlet and outlet pores for solving the steady state flow Eq. (1). A total pressure drop of 10 Pa was set across the network from the inlet to the outlet wall.

3.3.2.3. Boundary conditions for species transport. A Dirichlet boundary condition was established at the inlet wall determined by the initial state of charge (SOC) of the inlet solution, defined as:

$$\begin{aligned} \text{SOC} &= \frac{C_{II}}{C^{0-}} \\ C_{II}^{in} &= C^{0-} \cdot \text{SOC} \\ C_{III}^{in} &= C^{0-} \cdot (1 - \text{SOC}) \end{aligned} \quad (18)$$

where C_{II} corresponds to the concentration of V(II), C^{0-} is the total concentration of both vanadium species (i.e. V(II) and V(III)) present in the electrolyte, C_{II}^{in} and C_{III}^{in} are the concentrations of V(II) and V(III) at the inlet boundary, respectively.

At the outlet wall, a Newman condition of zero diffusive flux out of the system was established. Imposing an open boundary to the system of irregularly distributed pores required the addition of a layer of so-called “dummy pores” adjacent to the outlet pores. To achieve a zero diffusive flux in this connection, the concentration at the dummy pore was set equal to the concentration of the output pore.

3.3.2.4. Boundary conditions for charge transport. The boundary conditions at the walls were set as operating under potentiostatic conditions. A potential difference was set across the network by imposing Dirichlet boundaries of electrolyte potential at the inlet and outlet pores. The potential distribution at each pore was recalculated at every time-step in the transient simulation.

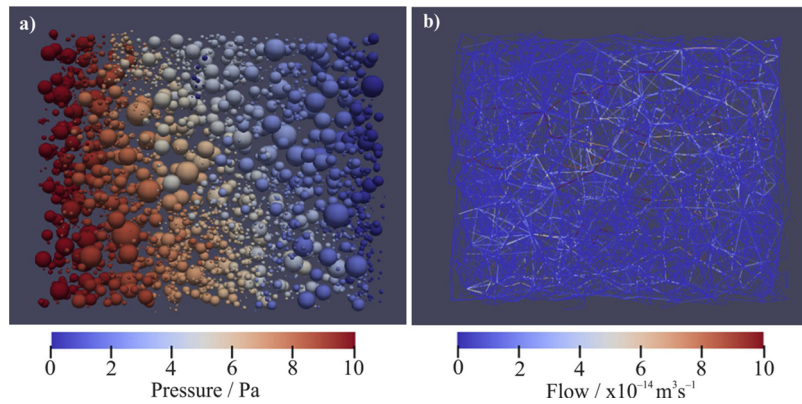


Fig. 5. Decoupled steady-state (a) pressure, and; (b) flow distributions.

3.3.3. Convective and diffusive species transport

Fig. 5 shows the decoupled steady-state pressure and flow distributions using pores and throats respectively. Fig. 5(a) shows the distribution of pressure at each of the pores in the network due to the pressure boundaries imposed at the inlet and outlet faces ($P_{in} = 10 \text{ Pa}$, $P_{out} = 0 \text{ Pa}$) and, (b) presents the distribution of flows through each of the throats. The solution of the pressure and flow profiles is achieved in 6 s. It is shown that the electrolyte flow is not uniformly distributed within the electrode, leading to regions in which the flow rate is close to zero and regions where the flow rate is maximum (i.e. $4.0 \times 10^{-13} \text{ m}^3 \text{s}^{-1}$).

The irregularity in flow distribution across the electrode draws “flow paths” through which the electrolyte will infiltrate the pores more rapidly. Such paths of maximum flow rate (red throats) represent the regions where the convective transport is dominant, rather than diffusion. On the other hand, the regions where the convective flow is minimum (blue throats), the transport of species would be dictated by the diffusive flux between pores. This is demonstrated by the analysis of the permeation of electrolyte with time, as shown in Fig. 6.

Initially (Fig. 6a), the concentration of vanadium species was close to zero (i.e. $C_{II}(0) = 0.001 \text{ mol m}^{-3}$) at every pore, except at the inlet pores, where it was set to $C_{II}^{in}(0) = 750 \text{ mol m}^{-3}$. As the simulation

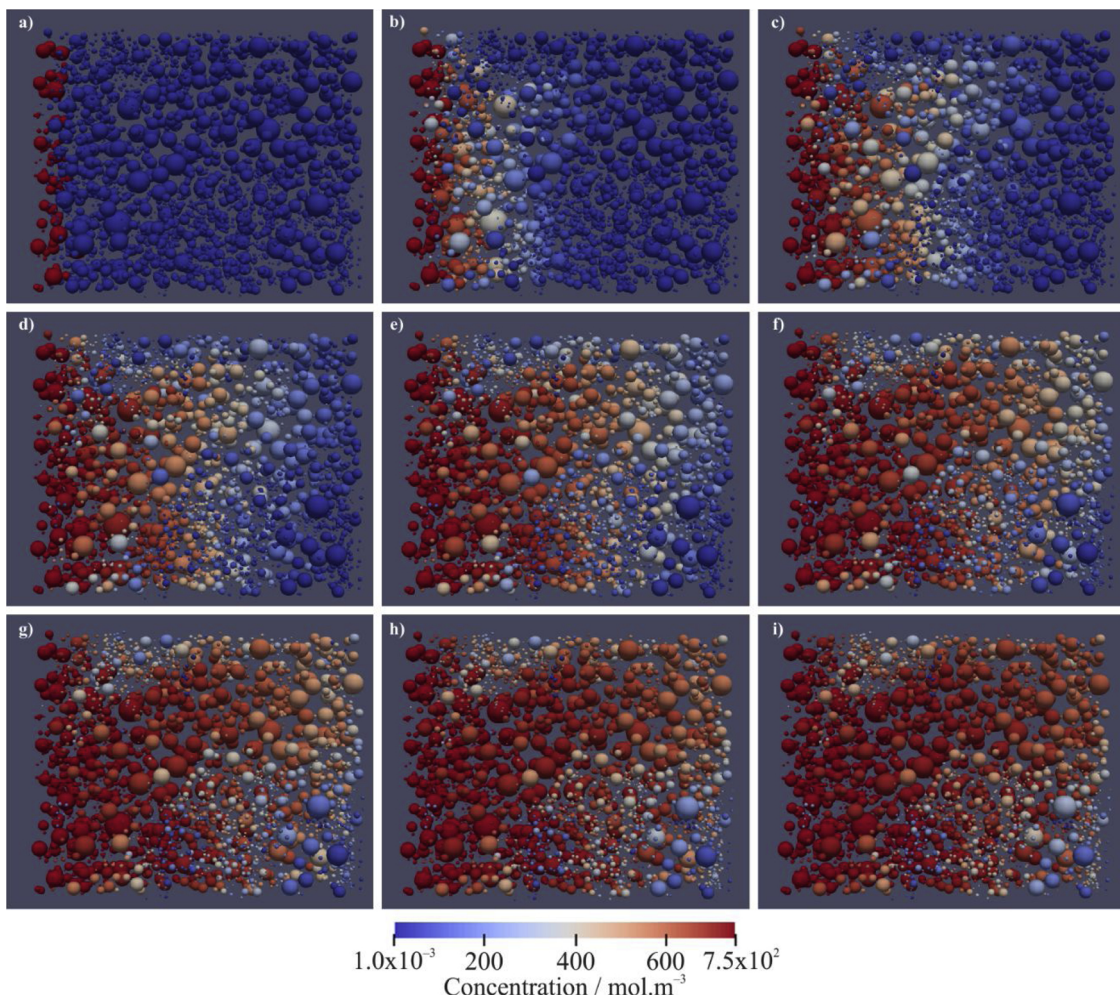


Fig. 6. Permeation of V(II) through a PNM representing a section of Toray 090. The 3D images proceed in 1 s steps starting from 0 s (a).

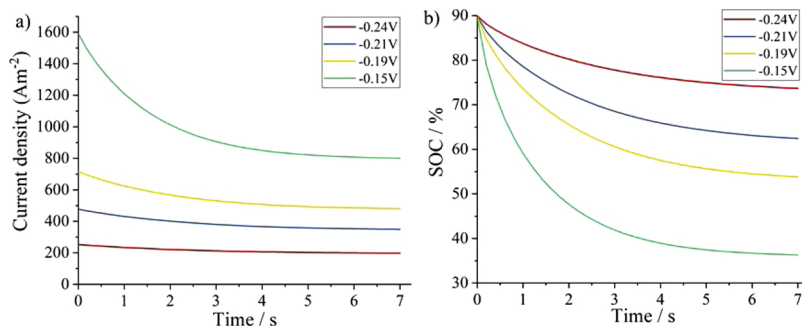


Fig. 7. (a) Current density; and, (b) state of charge variation with time at various electrode potential drops.

proceeds, the electrolyte primarily permeates the pores located along the path of maximum flow. Concentration changes due to diffusive flow began to be noticed when the electrolyte reached the outlet wall. The concentration in the regions which, until now had not been permeated with electrolyte, slowly starts to increase. The effect of an initially high convective flow enhanced a subsequent diffusive flux, since a higher concentration gradient between pores was imposed due to the convective flux. Despite the effect of both convection and diffusion, some pores remained largely untouched throughout the simulation. This non-uniform distribution of electrolyte has an impact on the battery performance since it implies a non-uniform utilisation of the electrode. These results are consistent with the work by Banerjee et al. which demonstrate that the electrolyte permeates the electrode pores in a non-uniform way, drawing flow paths that are dependent on the pore's connectivity and therefore the electrode internal structure [38].

3.3.4. Additional transient migration and reactive transport factors

In this section, a detailed analysis of the distribution of concentration and current density due to the presence of electrochemical reaction and migration is presented for the pore-network of the Toray 090 carbon paper sample. The steady-state simulation of the pressure and flow distributions converged after 9 s, while the coupled charge and species transport distributions converged after 16 min for each time-step in the simulation, using a single core of a HP workstation: Intel® Xeon® CPU E5-166-v3.

Fig. 7(a) shows the volume averaged values of current density in the anode under potentiostatic discharge at different averaged electrode potentials. The averaged electrode potentials are defined according to Qiu et al. [26] as the potential drop across the active surface area ($\varphi_s - \varphi_e$) at each pore in the simulation (Eq. (19)). These values are independent of concentration and therefore equilibrium potential, E_a .

$$\Delta\varphi = \frac{1}{np} \sum_i^{np} (\varphi_s - \varphi_{e,i}) \quad (19)$$

The simulations were run at four different values of average electrode potential difference across the solid–electrolyte interface: -0.15 V , -0.19 V , -0.21 V and -0.24 V .

As expected, lower current densities were obtained at more negative electrode potentials (e.g. -0.24 V) – thus lower overpotentials – and higher current densities at more positive electrode potentials (e.g. -0.15 V) – higher overpotentials. At more positive electrode potentials, a more significant drop in current density leads to a faster consumption of species. This is graphically represented in Fig. 7(b) where the SOC is plotted for different electrode potentials. For the most positive electrode potential (-0.15 V) – highest overpotentials – the electrode is discharged from 50% to 25% in 2.5 s, while at the most negative electrode potential (-0.24 V) – lowest overpotentials – the electrode only discharges 2.5% (to 47.5%) in the same amount of time.

The previous volume-averaged analysis offers insight into the relationship between parameters that play a key role on the cell performance (i.e. current density, cell potential and average SOC) at a macroscopic level. However, pore-scale results offer much more detail about species and current transport in VRFBs compared to volume-averaged methods.

Fig. 8 presents the pore-scale results of the current distribution across the electrode at 50% SOC under potentiostatic discharge at different electrode potentials (-0.24 V , -0.21 V , -0.19 V , -0.15 V). Analogous to the volume-averaged results, higher currents are obtained at more positive electrode potentials – higher overpotentials – but the pore-scale results obtained with the PNM simulation show that the distribution of current throughout the electrode is not uniform, in agreement with the LBM models Qiu et al. present [25]. This leads to

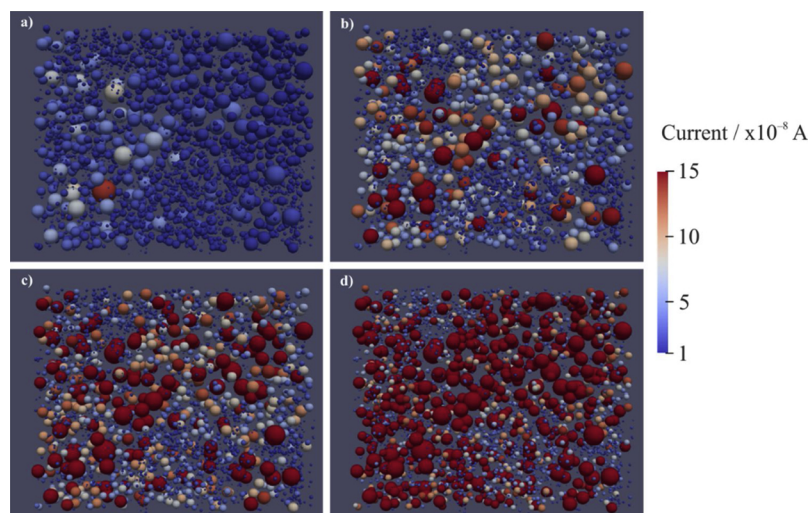


Fig. 8. Current distribution at various electrode potentials (a) -0.24 V , (b) -0.21 V , (c) -0.19 V and (d) -0.15 V (at 50% state of charge).

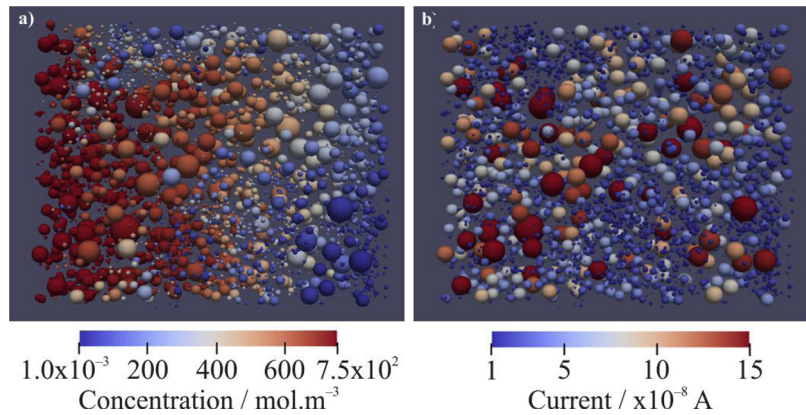


Fig. 9. (a) Current distribution (at -0.21 V electrode potential and state of charge 50%), and; (b) concentration (purely convective-diffusive regime) distribution after 4 s.

development of regions within the electrode that are more reactive than others and contribute to electrode performance to a greater extent.

A comparison between electrolyte concentration (under a purely convective-diffusive regime) and absolute current at each pore can be seen in Fig. 9. By comparing the location of pores where the absolute current is higher (Fig. 9a) with the concentration distribution in a purely convective-diffusive regime (Fig. 9b), it is seen that the ‘path’ of large pores correlates with the regions that are permeated by electrolyte

at a higher rate. This analysis shows that a PNM approach can give an insight into the local correlation of transport parameters (*i.e.* pore size, current and concentration distributions) at a pore-scale level. On the other hand, a volume averaged model only considers changes in the current and concentration distributions along the length of the cell. The results presented in this work with a PNM approach reinforce the findings of Qiu et al. which prove that the current density is non-uniformly distributed along the three-dimensional space [25]. It is

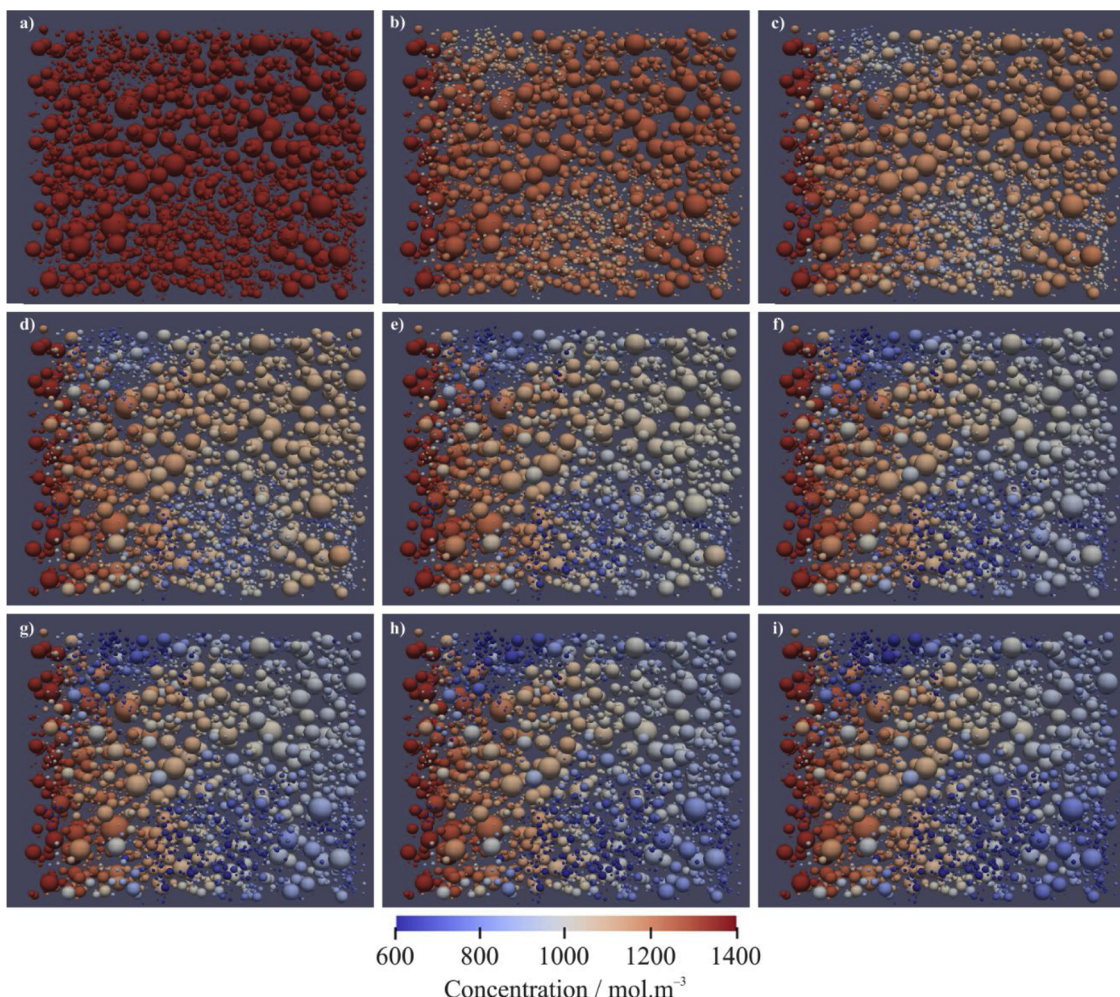


Fig. 10. Transient concentration distribution with electrochemical reaction with electrode potential of -0.21 V. The 3D images proceed in 1 s steps starting from 0 s (a) to 8 s (f).

important to mention here, that a larger pore size would imply a larger active surface area and the absolute current transfer to/from the solid interface is therefore directly influenced by the sizes of pores.

Furthermore, an analysis on the transient distribution of vanadium species is performed, with additional conditions whereby the concentration is influenced by convective, diffusive, reactive and migration transport conditions. Fig. 10 shows the concentration change with time for a potentiostatic discharge with electrode potential of -0.21 V and an initial SOC of 90%, corresponding to an initial concentration of species in all pores of $C_{\text{II}}(0) = 1350\text{ mol m}^{-3}$ (Fig. 10a). The inlet concentration, as stated in the methodology, is constant throughout the simulation with a value of $C_{\text{II}}^{\text{in}} = 1350\text{ mol m}^{-3}$ corresponding to 90% SOC.

As expected, it is shown that the concentration profile of V(II) is not uniform within the electrode. This leads to a non-uniform depletion of vanadium species across the electrode during discharge. It is therefore evident that a volume averaged value of the electrode SOC only poorly resembles the actual concentration distribution of species within the cell. This can be graphically shown by comparing Fig. 7(b) (volume-averaged results) with Fig. 10 (pore-scale results). At 4 s, the volume-averaged results give a SOC of 67.52%, while the pore-scale 3D results show areas in which the SOC significantly differs from this value.

In this context, Fig. 11 graphically represents the transient current density distribution across the electrode for a potentiostatic discharge with electrode potential of -0.21 V and an initial SOC of 90%. By comparing Fig. 10(a) and Fig. 11(a), it is clearly shown that when the

concentration of species is constant in the electrode, the gradient of the current density across the electrode is determined by the potential difference in the electrolyte from the inlet to the outlet. This result is in accordance with Eq. (11), since it implies that the second term on the RHS is zero. As the concentration of species changes with time due to convection, migration, reaction and diffusion, the second term of Eq. (11) presents a bigger influence on the current density distribution.

Figs. 10 and 11 show that the starvation of electrolyte in certain pores due to the pore size distribution leads to a non-even rate of discharge and current density distribution throughout the electrode. This causes to the existence of areas within the electrode which are more utilised than others and therefore contribute to a higher extent to the fast discharge of the battery.

A more direct comparison can be made by comparing the results of a transient concentration change when the system is under pure convective-diffusive transport and when the system is influenced by electrochemically reactive and migratory processes (Fig. 12). It is shown that the regions where convective flow is dominant (*i.e.* rapidly permeated by electrolyte) result in a lower rate of V(II) depletion than the regions where the electrolyte permeation is slower. As previously analysed, these regions also correspond to the sites with higher values of transfer current (Fig. 9). One possible reason for this is that, because of the effect of a higher convective flux into these pores, the sites would continuously be replenished with fresh electrolyte before all the existing V(II) is consumed, enhancing the electrochemical reaction.

In an analogous way, the pores that present a limited convective

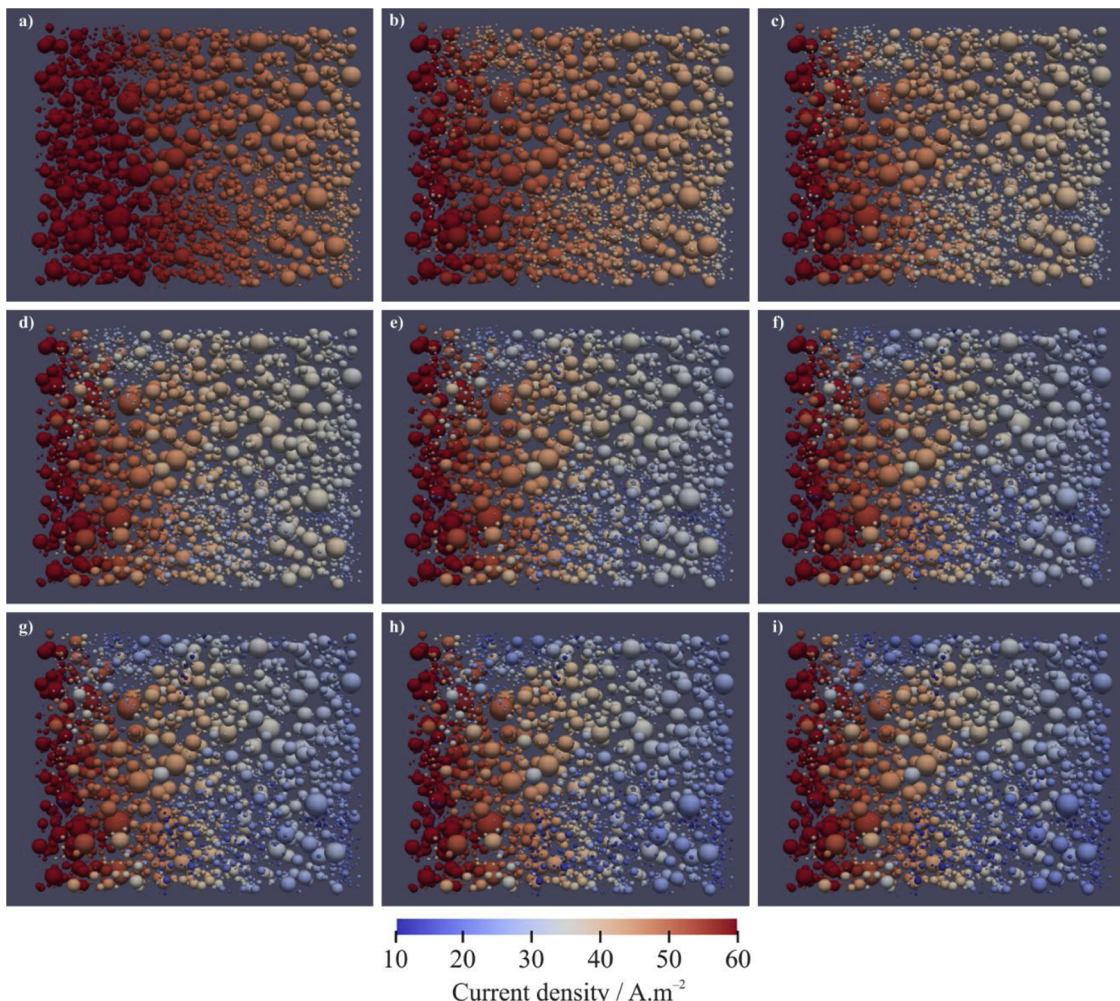


Fig. 11. Transient current density distribution with electrochemical reaction with electrode potential of -0.21 V . The 3D images proceed in 1 s steps starting from 0 s (a) to 8 s (f).

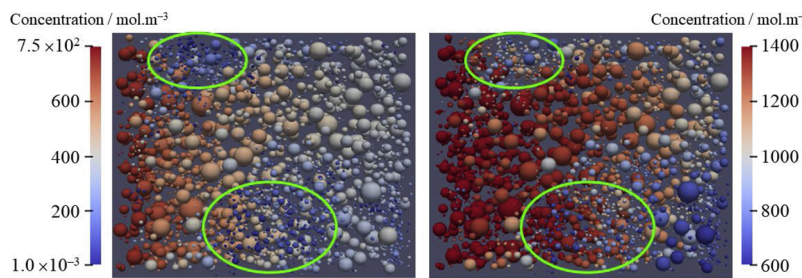


Fig. 12. Comparison of concentration distribution at 5 s in (a) a purely convective-diffusive transport system and, (b) a convective-diffusive transport system with electrochemical migration. Green rings highlight the regions where convective flow is limited. (For interpretation of the references to colour in this figure legend, the reader is referred to the web version of this article.)

transport (highlighted by the green rings in Fig. 12(a)) are also the ones that present a faster rate of depletion of vanadium species. This implies that the sites where the flow is minimum are discharged at a higher rate than the sites with high convective flow. The existence of these ‘clusters of pores’ where limited convective transport is dominant leads to a faster rate of discharge of the cell as a whole. As the concentration of V (II) in these pores tends to zero, the effect of diffusion becomes dominant: the concentration gradient between two pores of very different concentration increases and therefore becomes more significant than the convective or migration terms. This effect of the non-uniform distribution of species on the depletion of vanadium species could be interpreted as one of the factors that influence a fast discharge in RFB electrodes.

3.4. Comparison of pore-scale models in terms of computational expense

As a final remark, useful insight can be drawn by comparing the computational expense associated with the model presented in this work with the one by Qiu et al. [25] (a) and Qiu et al. [26] (b). The first sample analysed by Qiu et al. is a geometric subset from an original master X-CT structure. The subset occupies a volume of dimensions $600 \times 150 \times 600 \mu\text{m}^3$, and a specific surface area of $39,700 \text{ m}^{-1}$. Qiu et al. implement an LBM to solve the flow field within the electrolyte, and a fully implicit 3D FVM to solve the coupled charge and species transport equations in the pore-space domain. The authors implement the LBM and FVM methods in FORTRAN 90 using the Message Passing Interface for parallel processing. The simulation for this subset of the X-CT structure is reported to converge in 20 h using a 64-core computer running on the TeraGrid.

The second work presented by Qiu et al. [26] analyses three different electrode structures reconstructed from X-CT images. All structures occupy a volume of dimensions $900 \times 135 \times 450 \mu\text{m}^3$, and specific surface areas of $37,500 \text{ m}^{-1}$, $47,700 \text{ m}^{-1}$ and $69,700 \text{ m}^{-1}$. Analogous to the first case [25], LBM and FVM were implemented to solve the flow field and coupled charge and species transport within the electrolyte respectively. All simulations are reported to converge within 20 h using a 112-core cluster running on the NSF XSEDE system [26].

The PNM approach presented in this work analyses a network extracted from X-CT images with dimensions reported in Table 3 and specific surface area of $41,062 \text{ m}^{-1}$. The steady-state flow equations were solved with a successive over relaxation method and the transient coupled charge and species transport were solved with an explicit Euler scheme. The flow equations converged in 9 s and the species transport in 16 min for each time-step outputted from the simulation. The system was solved using a single core of a HP workstation: Intel® Xeon® CPU E5-166-v3.

4. Conclusions and future work

In this work, a framework based on a pore-network model is introduced to simulate the coupled flow, species and charge transport that occur within electrodes in electrochemical devices. This work represents a bridge between volume-averaged models that simulate the transport processes in a continuum space, and pore-scale models which

perform direct numerical simulations over X-CT reconstructed images. The main advantage of this model is its ability to visually represent the concentration and current distributions inside the electrode within a reasonably low computational time. Furthermore, it presents the ability to capture the effect of the electrode geometry on the flow, concentration and current distributions. This information will aid in the design and optimisation of electrodes for electrochemical devices.

The methodology presented in this work is based on an MCM approach using an explicit Euler scheme for obtaining the transient concentration distributions as a function of convection, diffusion, migration and electrochemical reaction. The methodology was validated with a cubic hypothetical PNM built with OpenPNM representing an anode with a specific surface area of $16,200 \text{ m}^{-1}$. By comparing the steady-state electrode potential and overpotential of this system as a function of SOC (Fig. 2), with the results presented by You et al. [55] it is shown that the values predicted with the present model are consistent with the values reported in the literature for continuum models and experimental results.

As a case study, the algorithm was implemented over a pore-network extracted from an X-CT data of a Toray 090 sample. The results show that the pore-size distribution representing the electrode void space is directly related to the flow, concentration and current distribution within the network. An analysis of the current distribution shows that it is not uniform throughout the network, leading to areas in which the current output is almost ten times higher than elsewhere. This proves the advantage of using a pore-scale model over a continuous volume-averaged one for representing more accurately the effects of transport processes in electrode utilisation. The flow profile results show the existence of routes within the electrode through which the convective flow of electrolyte is minimum. These areas are therefore mass transport limited as the movement of species is almost purely diffusive. Since the pores on these routes are not constantly replenished with fresh electrolyte, they will discharge at a faster rate than the pores on routes with high convective flow. This leads to two major conclusions: (a) the SOC is not uniform across the electrode, and; (b) the effect of mass-transport limited areas in the electrode leads to a faster discharge. These results represent the first visual showcase of how regions limited by low convective flow affect the rate of discharge in an electrode.

In terms of computational expense, the results show that the framework presented in this work based on a PNM approach is significantly less expensive than the previous works presented by Qiu et al. which use a LBM coupled with a FVM [25,26]. The PNM approach converges within 16 min on a standard single core workstation, while the LBM-FVM simulations converge in 20 h running on a cluster. This represents a significant advantage of the present model over existing models since it has the ability to simulate the coupled flow, species and charge transport distributions at a pore-scale within the electrode without requiring a high processing power.

As a drawback of this model, the network that constitutes the electrode geometry is dependent on the pore-network extraction algorithm used. Furthermore, the active surface area is estimated based on an approximation of the pore phase with a simplified geometry. As shown in Fig. 1, the idealisation of the microstructure could lead to the

over or under estimation of the real surface area. If the actual surface area is unknown, an approximation based on the PNM approach extracted from X-CT – reconstructed geometry will lead to a fair prediction of the concentration, potentials and current distributions within an electrode, since the flow prediction is accurate based on a comparison with permeability data. If the experimental surface area is provided, the PNM could be updated with a “correction factor” over the surface area of each pore. This would increase or decrease the term $S_{A,i}$ in the exchange current (Eq. (6)) but the methodology, and therefore the convergence speed, would not be altered.

It must be emphasised that the segmented image of Toray090 used in this work does not represent a REV of the whole electrode. A REV analysis falls beyond the purpose of this paper. The purpose of using an X-CT image is to show the capabilities of the model when implemented in a real system.

Future work will analyse the effect of different flow rates (*i.e.* pressure drops) in the electrode potential, current distribution and

Appendix 1

Refer to Fig. A1 for a flow chart that graphically outlines the numerical algorithm implemented in this work.

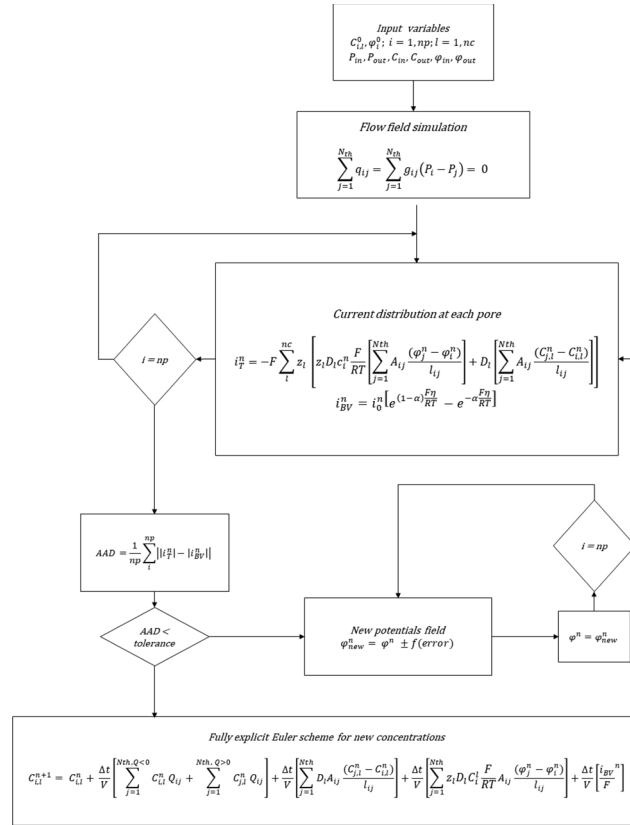


Fig. A1. Flow chart graphically outlining the numerical algorithm.

Appendix 2 Validation and analytical solution of Eq. (10)

This section presents the analytical solution of the MCM for (mass) transport of species influenced by convection, diffusion, migration and reaction in a pore network of eight pores connected in series. The following assumptions were made:

- All pores have the same volume: $V_1 = V_2 = V$.
- All connecting throats have the same cross-section area ($A_{ij} = A$) and length ($L_{ij} = L$), thus the volumetric flow rate between pores is the same for all throats: *i.e.* $Q_{12} = Q_{23} = Q$.
- The potential gradient between pores is equal for all connections: $\Delta\varphi_{12} = \Delta\varphi_{23} = \Delta\varphi$.
- The system is operating under limiting current conditions.
- No diffusive flux out of the pores is considered.

- Dirichlet boundary conditions are assumed at the inlet and outlet pores. The concentration at the inlet pore is set to $C_{in} = 10 \text{ mol m}^{-3}$, and the concentration at the outlet pore is $C_{out} = 0 \text{ mol m}^{-3}$.

The MCM for the transient transport of V(II) (represented by l) is:

$$V_l \frac{dC_i^l}{dt} = \sum_{j=1}^{N_{th}q < 0} C_i^l q_{ij} + \sum_{j=1}^{N_{th}q > 0} C_i^l q_{ij} + \sum_{j=1}^{N_{th}} D_l A_{ij} \frac{(C_j^l + C_i^l)}{l_{ij}} + \sum_{j=1}^{N_{th}} z_l D_l C_i^l \frac{F}{RT} A_{ij} \frac{(\varphi_j - \varphi_i)}{l_{ij}} + S(C_i^l) \quad (\text{A1})$$

For simplicity, the concentration C_i^l will be written as C_i . Since the hypothetical system consists of pores connected in series, Eq. (A1) can be rewritten as:

$$V_l \frac{dC_i}{dt} = C_{i-1} Q_{i,i-1} - C_i Q_{i,i+1} + D_l A \frac{(C_{i-1} - C_i)}{L} + Z_l D_l C_i \frac{F}{RT} A \frac{2\Delta\varphi}{L} + S(C_i) \quad (\text{A2})$$

Based on the assumption that all pores have the same size and all flows are equal, Eq. (A2) can be rewritten in terms of a characteristic time $\tau = V/Q$ as:

$$\frac{dC_i}{dt} = \frac{1}{\tau} (C_{i-1} - C_i) + D_l A \frac{(C_{i-1} - C_i)}{LA} + Z_l D_l C_i \frac{F}{RT} A \frac{2\Delta\varphi}{LV} + \frac{S(C_i)}{V} \quad (\text{A3})$$

Since the system is working under limiting current conditions, the source/sink term of the mass transport is defined as:

$$S(C_i) = \frac{-i_l S_A}{F} \quad (\text{A4})$$

where S_A represents the active surface area of each pore, F is the Faraday constant and i_l is the limiting current:

$$i_l = z_l F k_m C_i \quad (\text{A5})$$

All constants in the equations can be renamed as follows:

$$\alpha = \frac{1}{\tau} + \frac{D_l A}{LV} \quad (\text{A6})$$

$$\beta = \frac{2z_l D_l F A}{RT LV} \Delta \quad (\text{A7})$$

$$\gamma = \frac{z_l k_m S_A}{V} \quad (\text{A8})$$

$$\lambda = -\beta + \alpha + \gamma \quad (\text{A9})$$

The analytical solution of Eq. (A3) is solved as an infinite series, considering that the initial concentration of species in all pores is zero, and the concentration change with time is defined by a step input which remains constant through time:

$$C_0 = 10 \begin{cases} t = 0 \\ t > 0 \end{cases} \quad (\text{A10})$$

Thus, the analytical solution for the concentration as a function of time for the N th pore is:

$$\frac{C_N}{C_0} = \frac{\alpha^N}{\lambda^N} \left(1 - e^{-\lambda t} \sum_{n=1}^N \frac{\lambda^{n-1} t^{n-1}}{(n-1)!} \right) \quad (\text{A11})$$

Comparison of the analytical solution with the explicit Euler scheme based on the same assumptions.

[Fig. A2](#)

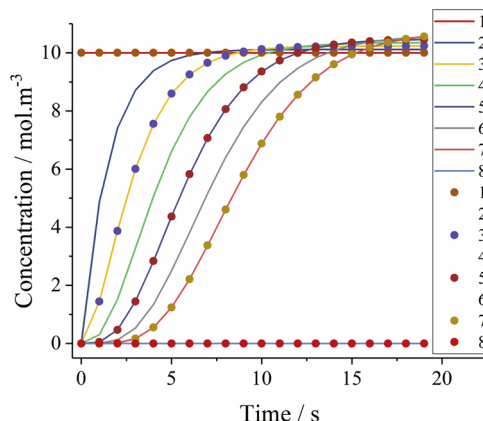


[Fig. A2](#). Validation of explicit Euler scheme with analytical solution for an eight-pore system (lines represent analytical solution, points represent Euler scheme).

Appendix 3. Nomenclature

Symbol	Description	Units
A	Cross sectional area	m^2
AAD	Absolute average deviation	—
A_e	Specific surface area	m^{-1}
C	Concentration	mol m^{-3}
D_L	Dispersion coefficient	$\text{m}^2 \text{s}^{-1}$
D_e	Effective diffusivity	$\text{m}^2 \text{s}^{-1}$
E	Effective potential	V
E^0	Equilibrium potential	V
F	Faraday constant	A s mol^{-1}
g	Hydraulic conductivity	$\text{m}^3 \text{s}^{-1} \text{Pa}^{-1}$
i_0	Exchange current	A
i_{BV}	Current from Butler–Volmer	A
i_t	Transfer current	A
J_{ext}	External current density	A m^{-2}
k_a	Standard reaction rate constant	m s^{-1}
K	Permeability	m^2
l	Throat length	m
L	Half-cell width/electrode thickness	m
MCM	Mixed cell method	—
N_p	Number of pores	—
N_t	Number of throats	—
P	Pressure	Pa
PNM	Pore network model	—
q	Flow rate	$\text{m}^3 \text{s}^{-1}$
R	Universal gas constant	$\text{J mol}^{-1} \text{K}^{-1}$
Re	Reynolds number	—
r_p	Pore radius	m
r_t	Throat radius	m
S_A	Active surface area	m^2
SOC	State of charge	—
t	Time	s
T	Operating temperature	K
u_{av}	Average electrolyte velocity	m s^{-1}
V	Volume	m^3
z	Valence	—
<i>Greek letters</i>		
α_-	Anodic transfer coefficient	—
α_+	Cathodic transfer coefficient	—
Δ	Difference	—
η	Overpotential	V
μ	Viscosity	Pas
φ	Potential	V

References

- [1] M.H. Chakrabarti, N.P. Brandon, S.A. Hajimolana, F. Tariq, V. Yufit, M.A. Hashim, M.A. Hussain, C.T.J. Low, P.V. Aravind, Application of carbon materials in redox flow batteries, *J. Power Sources* 253 (2014) 150–166, <https://doi.org/10.1016/J.JPOWSOUR.2013.12.038>.
- [2] G. Wei, C. Jia, J. Liu, C. Yan, Carbon felt supported carbon nanotubes catalysts composite electrode for vanadium redox flow battery application, *J. Power Sources* 220 (2012) 185–192, <https://doi.org/10.1016/J.JPOWSOUR.2012.07.081>.
- [3] A.-Q. Su, N.-F. Wang, S.-Q. Liu, T. Wu, S. Peng, Modification of carbon paper electrode via hydrothermal oxidation applied in the vanadium redox battery, *Acta Physico-Chim. Sin.* 28 (2012) 1387–1392, <https://doi.org/10.3866/PKU.WHXB201204013>.
- [4] B. Sun, M. Skyllas-Kazacos, Modification of graphite electrode materials for vanadium redox flow battery application—I. Thermal treatment, *Electrochim. Acta* 37 (1992) 1253–1260, [https://doi.org/10.1016/0013-4686\(92\)85064-R](https://doi.org/10.1016/0013-4686(92)85064-R).
- [5] B. Chakrabarti, D. Nir, V. Yufit, F. Tariq, J. Rubio-Garcia, R. Maher, A. Kucernak, P.V. Aravind, N.P. Brandon, Performance enhancement of reduced graphene oxide-modified carbon electrodes for vanadium redox-flow systems, *ChemElectroChem* 4 (2017) 194–200, <https://doi.org/10.1002/celc.201600402>.
- [6] Z. He, Z. Chen, W. Meng, Y. Jiang, G. Cheng, L. Dai, L. Wang, Modified carbon cloth as positive electrode with high electrochemical performance for vanadium redox flow batteries, *J. Energy Chem.* 25 (2016) 720–725, <https://doi.org/10.1016/j.jec.2016.04.002>.
- [7] X.L. Zhou, Y.K. Zeng, X.B. Zhu, L. Wei, T.S. Zhao, A high-performance dual-scale porous electrode for vanadium redox flow batteries, *J. Power Sources* 325 (2016) 329–336, <https://doi.org/10.1016/j.jpowsour.2016.06.048>.
- [8] X.L. Zhou, T.S. Zhao, Y.K. Zeng, L. An, L. Wei, A highly permeable and enhanced surface area carbon-cloth electrode for vanadium redox flow batteries, *J. Power Sources* 329 (2016) 247–254, <https://doi.org/10.1016/j.jpowsour.2016.08.085>.
- [9] R. Scipioni, P.S. Jørgensen, C. Graves, J. Hjelm, S.H. Jensen, A physically-based equivalent circuit model for the impedance of a LiFePO₄/Graphite 26650 cylindrical cell, *J. Electrochim. Soc.* 164 (2017) A2017–A2030, <https://doi.org/10.1149/2.1071709jes>.
- [10] N. Ogihara, S. Kawachi, C. Okuda, Y. Itou, Y. Takeuchi, Y. Ukyo, Theoretical and experimental analysis of porous electrodes for lithium-ion batteries by electrochemical impedance spectroscopy using a symmetric cell, *J. Electrochim. Soc.* 159 (2012) A1034–A1039, <https://doi.org/10.1149/2.057207jes>.
- [11] J. Huang, J. Zhang, Theory of impedance response of porous electrodes: simplifications, inhomogeneities, non-stationarities and applications, *J. Electrochim. Soc.* 163 (2016) A1983–A2000, <https://doi.org/10.1149/2.0901609jes>.
- [12] R. de Levie, On porous electrodes in electrolyte solutions, *Electrochim. Acta* 8 (1963) 751–780, [https://doi.org/10.1016/0013-4686\(63\)80042-0](https://doi.org/10.1016/0013-4686(63)80042-0).
- [13] D. Qu, Fundamental principals of battery design: porous electrodes, *AIP Conf. Proc.* 1597 (2014) 66, <https://doi.org/10.1063/1.4878477>.
- [14] J.P. Meyers, M. Doyle, R.M. Darling, J. Newman, The impedance response of a porous electrode composed of intercalation particles, *J. Electrochim. Soc.* 147 (2000) 2930–2940, <https://doi.org/10.1149/1.1393627>.
- [15] A.A. Shah, M.J. Watt-Smith, F.C. Walsh, A dynamic performance model for redox-flow batteries involving soluble species, *Electrochim. Acta* 53 (2008) 8087–8100, <https://doi.org/10.1016/J.ELECTACTA.2008.05.067>.
- [16] A.A. Shah, R. Tangirala, R. Singh, R.G.A. Wills, F.C. Walsh, A dynamical unit cell model for the all-vanadium flow battery, *J. Electrochim. Soc.* 158 (2011) A671–A677, <https://doi.org/10.1149/1.3561426>.
- [17] I.M. Bayanov, R. Vanhaelst, The numerical simulation of vanadium RedOx flow batteries, *J. Math. Chem.* 49 (2011) 2013–2031, <https://doi.org/10.1007/s10910-011-9872-x>.
- [18] Q. Zheng, X. Li, Y. Cheng, G. Ning, F. Xing, H. Zhang, Development and perspective in vanadium flow battery modeling, *Appl. Energy* 132 (2014) 254–266, <https://doi.org/10.1016/j.apenergy.2014.06.077>.
- [19] Q. Xu, T.S. Zhao, Fundamental models for flow batteries, *Prog. Energy Combust. Sci.* 49 (2015) 40–58, <https://doi.org/10.1016/j.pecs.2015.02.001>.
- [20] Y.A. Gandomi, D.S. Aaron, T.A. Zawodzinski, M.M. Mench, In situ potential

- distribution measurement and validated model for all-vanadium redox flow battery, *J. Electrochem. Soc.* 163 (2016) A5188–A5201, <https://doi.org/10.1149/2.0211601jes>.
- [21] A.Z. Weber, J. Newman, Modeling transport in polymer-electrolyte fuel cells, *Chem. Rev.* 104 (2004) 4679–4726, <https://doi.org/10.1021/cr0207291>.
- [22] C. Siegel, Review of computational heat and mass transfer modeling in polymer-electrolyte-membrane (PEM) fuel cells, *Energy* 33 (2008) 1331–1352, <https://doi.org/10.1016/j.energy.2008.04.015>.
- [23] A.A. Shah, K.H. Luo, T.R. Ralph, F.C. Walsh, Recent trends and developments in polymer electrolyte membrane fuel cell modelling, *Electrochim. Acta* 56 (2011) 3731–3757, <https://doi.org/10.1016/j.electacta.2010.10.046>.
- [24] A.Z. Weber, M.M. Mench, J.P. Meyers, P.N. Ross, J.T. Gostick, Q. Liu, Redox flow batteries: a review, *J. Appl. Electrochem.* 41 (2011) 1137–1164, <https://doi.org/10.1007/s10800-011-0348-2>.
- [25] G. Qiu, A.S. Joshi, C.R. Dennison, K.W. Knehr, E.C. Kumbur, Y. Sun, 3-D pore-scale resolved model for coupled species/charge/fluid transport in a vanadium redox flow battery, *Electrochim. Acta* 64 (2012) 46–64, <https://doi.org/10.1016/J.ELECTACTA.2011.12.065>.
- [26] G. Qiu, C.R. Dennison, K.W. Knehr, E.C. Kumbur, Y. Sun, Pore-scale analysis of effects of electrode morphology and electrolyte flow conditions on performance of vanadium redox flow batteries, *J. Power Sources* 219 (2012) 223–234, <https://doi.org/10.1016/J.JPOWSOUR.2012.07.042>.
- [27] M. Rebai, M. Prat, Scale effect and two-phase flow in a thin hydrophobic porous layer. Application to water transport in gas diffusion layers of proton exchange membrane fuel cells, *J. Power Sources* 192 (2009) 534–543, <https://doi.org/10.1016/J.JPOWSOUR.2009.02.090>.
- [28] X. Yang, Y. Mehmani, W.A. Perkins, A. Pasquali, M. Schönher, K. Kim, M. Perego, M.L. Parks, N. Trask, M.T. Balhoff, M.C. Richmond, M. Geier, M. Krafczyk, L.-S. Luo, A.M. Tartakovsky, T.D. Scheibe, Intercomparison of 3D pore-scale flow and solute transport simulation methods, *Adv. Water Resour.* 95 (2016) 176–189, <https://doi.org/10.1016/J.ADVWATRES.2015.09.015>.
- [29] S.V. Patankar, Numerical Heat Transfer and Fluid Flow, CRC Press, 1980 <https://www.crcpress.com/Numerical-Heat-Transfer-and-Fluid-Flow/Patankar/p/book/9780891165224>. (Accessed 6 August 2018).
- [30] M.A.A. Spaid, F.R.J. Phelan, Lattice Boltzmann methods for modeling microscale flow in fibrous porous media, *Phys. Fluids* 9 (1997) 2468–2474, <https://doi.org/10.1063/1.869392>.
- [31] J.J. Monaghan, Smoothed particle hydrodynamics, *Annu. Rev. Astron. Astrophys.* 30 (1992) 543–574 www.annualreviews.org. (Accessed 6 August 2018).
- [32] M.J. Blunt, Multiphase Flow in Permeable Media: A Pore-Scale Perspective, 1st edition, Cambridge University Press, 2017 <http://admin.cambridge.org/academic/subjects/earth-and-environmental-science/applied-geoscience-petroleum-and-mining-geoscience/multiphase-flow-permeable-media-pore-scale-perspective>. (Accessed 6 August 2018).
- [33] B. Bijeljic, M.J. Blunt, Pore-scale modeling of transverse dispersion in porous media, *Water Resour. Res.* 43 (2007) W12511, <https://doi.org/10.1029/2006WR005700>.
- [34] P.A. García-Salaberri, I.V. Zenyuk, A.D. Shum, G. Hwang, M. Vera, A.Z. Weber, J.T. Gostick, Analysis of representative elementary volume and through-plane regional characteristics of carbon-fiber papers: diffusivity, permeability and electrical/thermal conductivity, *Int. J. Heat Mass Transf.* 127 (2018) 687–703, <https://doi.org/10.1016/J.IJHEATMASSTRANSFER.2018.07.030>.
- [35] J. Park, M. Matsubara, X. Li, Application of lattice Boltzmann method to a micro-scale flow simulation in the porous electrode of a PEM fuel cell, *J. Power Sources* 173 (2007) 404–414, <https://doi.org/10.1016/J.JPOWSOUR.2007.04.021>.
- [36] J.T. Gostick, M.A. Ioannidis, M.W. Fowler, M.D. Pritzker, Pore network modeling of fibrous gas diffusion layers for polymer electrolyte membrane fuel cells, *J. Power Sources* 173 (2007) 277–290, <https://doi.org/10.1016/J.JPOWSOUR.2007.04.059>.
- [37] M. Aghighi, M.A. Hoeh, W. Lehnert, G. Merle, J.T. Gostick, Simulation of a full fuel cell membrane electrode assembly using pore network modeling, *J. Electrochem. Soc.* 163 (2016) F384–F392, <https://doi.org/10.1149/2.0701605jes>.
- [38] R. Banerjee, N. Bevilacqua, L. Eifert, R. Zeis, Characterization of carbon felt electrodes for vanadium redox flow batteries – a pore network modeling approach, *J. Energy Storage* 21 (2019) 163–171, <https://doi.org/10.1016/J.JEST.2018.11.014>.
- [39] J. Gostick, M. Aghighi, J. Hinebaugh, T. Tranter, M.A. Hoeh, H. Day, B. Spellacy, M.H. Sharqawy, A. Bazylak, A. Burns, W. Lehnert, A. Putz, OpenPNM: a pore network modeling package, *Comput. Sci. Eng.* 18 (2016) 60–74, <https://doi.org/10.1109/MCSE.2016.49>.
- [40] Y. Mehmani, M. Oostrom, M.T. Balhoff, A streamline splitting pore-network approach for computationally inexpensive and accurate simulation of transport in porous media, *Water Resour. Res.* 50 (2014) 2488–2517, <https://doi.org/10.1002/2013WR014984>.
- [41] J. Tansey, M.T. Balhoff, Pore network modeling of reactive transport and dissolution in porous media, *Transp. Porous Media* 113 (2016) 303–327, <https://doi.org/10.1007/s11242-016-0695-x>.
- [42] R.C. Acharya, S.E.A.T.M. Van der Zee, A. Leijnse, Transport modeling of nonlinearly adsorbing solutes in physically heterogeneous pore networks, *Water Resour. Res.* 41 (2005) W02020, <https://doi.org/10.1029/2004WR003500>.
- [43] L. Li, C.A. Peters, M.A. Celia, Upscaling geochemical reaction rates using pore-scale network modeling, *Adv. Water Resour.* 29 (2006) 1351–1370, <https://doi.org/10.1016/J.ADVWATRES.2005.10.011>.
- [44] Q. Xiong, T.G. Baychev, A.P. Jivkov, Review of pore network modelling of porous media: experimental characterisations, network constructions and applications to reactive transport, *J. Contam. Hydrol.* 192 (2016) 101–117, <https://doi.org/10.1016/J.JCONHYD.2016.07.002>.
- [45] D. Kim, C.A. Peters, W.B. Lindquist, Upscaling geochemical reaction rates accompanying acidic CO₂-saturated brine flow in sandstone aquifers, *Water Resour. Res.* 47 (2011) W01505, <https://doi.org/10.1029/2010WR009472>.
- [46] Y. Mehmani, T. Sun, M.T. Balhoff, P. Eichhubl, S. Bryant, Multiblock pore-scale modeling and upscaling of reactive transport: application to carbon sequestration, *Transp. Porous Media* 95 (2012) 305–326, <https://doi.org/10.1007/s11242-012-0044-7>.
- [47] D.F. Yule, W.R. Gardner, Longitudinal and transverse dispersion coefficients in unsaturated plainfield sand, *Water Resour. Res.* 14 (1978) 582–588, <https://doi.org/10.1029/WR014i004p00582>.
- [48] Z. Yang, J. Zhang, M.C.W. Kintner-Meyer, X. Lu, D. Choi, J.P. Lemmon, J. Liu, Electrochemical energy storage for green grid, *Chem. Rev.* 111 (2011) 3577–3613, <https://doi.org/10.1021/cr100290v>.
- [49] IRENA, Renewable Energy Statistics 2018, Renewable Energy Statistics, 2018 <http://www.irena.org/publications/2018/Jul/Renewable-Energy-Statistics-2018>. (Accessed 14 August 2018).
- [50] M. Kazacos, M. Skyllas-Kazacos, Performance characteristics of carbon plastic electrodes in the all-vanadium redox cell, *J. Electrochem. Soc.* 136 (1989) 2759–2760 <http://jes.ecsl.org/content/136/9/2759.full.pdf>. (Accessed 6 August 2018).
- [51] M.L. Perry, R.M. Darling, R. Zaffou, High power density redox flow battery cells, *ECS Trans.* 53 (2013) 7–16, <https://doi.org/10.1149/05307.0007ecst>.
- [52] M.L. Perry, A.Z. Weber, Advanced redox-flow batteries: a perspective, *J. Electrochem. Soc.* 163 (2016) A5064–A5067, <https://doi.org/10.1149/2.01601jes>.
- [53] Grid Energy Storage – U.S. Department of Energy, December 2013, n.d. <https://www.energy.gov/oe/downloads/grid-energy-storage-december-2013>. (Accessed 13 August 2018).
- [54] “Joint EASE/EERA recommendations for a European Energy Storage Technology Development Roadmap towards 2030, The European Association for Storage of Energy (EASE),” n.d. <https://www.eera-set.eu/wp-content/uploads/148885-EASE-recommendations-Roadmap-04.pdf>.
- [55] D. You, H. Zhang, J. Chen, A simple model for the vanadium redox battery, *Electrochim. Acta* 54 (2009) 6827–6836, <https://doi.org/10.1016/J.electacta.2009.06.086>.
- [56] E. Sum, M. Skyllas-Kazacos, A study of the V(II)/V(III) redox couple for redox flow cell applications, *J. Power Sources* 15 (1985) 179–190 https://ac.els-cdn.com/0378775385800719/1-s2.0-0378775385800719-main.pdf?_tid=39c782c0-8e6b-47e9-97d4-61e7cf249a74&acdnat=1537705934_45398bf3ed0879edb44c90861881d93. (Accessed 23 September 2018).
- [57] T. Yamamura, N. Watanabe, T. Yano, Y. Shiokawa, Electron-transfer kinetics of $\text{Np}^{3+}/\text{Np}^{4+}$, $\text{NpO}_2^{+}/\text{NpO}_2^{2+}$, $\text{V}^{2+}/\text{V}^{3+}$, and $\text{VO}^{2+}/\text{VO}^{2+}$ at carbon electrodes, *J. Electrochem. Soc.* 152 (2005) A830–A836, <https://doi.org/10.1149/1.1870794>.
- [58] Y. Zhu, C. Huang, An improved median filtering algorithm for image noise reduction, *Phys. Procedia* 25 (2012) 609–616, <https://doi.org/10.1016/j.phpro.2012.03.133>.